High Power Diode Laser (HPDL) surface treatments to improve the mechanical properties and the corrosion behaviour of Mg-Zn-Ca alloys for biodegradable implants

N. Pulido-González[a,*], B. Torres[a], M. L. Zheludkevich[b], J. Rams[a]

[a] *Departamento de Matemática Aplicada, Ciencia e Ingeniería de Materiales y Tecnología Electrónica, ESCET, Universidad Rey Juan Carlos, C/ Tulipán s/n, 28933, Móstoles, Madrid, Spain*
[b] *MagIC-Magnesium Innovation Centre, Institute of Materials Research, Helmholtz-Zentrum Geesthacht, Max-Planck-Str. 1, 21502 Geesthacht, Germany*

Abstract

Biodegradability, low density and mechanical properties close to those of the bone are some of the intrinsic properties of the Mg-Zn-Ca alloys that have attracted significant attention for developing biodegradable implants. However, rapid degradation constitutes the main disadvantage of these alloys. In this work, two different alloys, Mg-1Zn-1Ca and Mg-3Zn-0.4Ca, were laser surface treated using a HPDL to increase hardness and to improve the corrosion performance. Depending on the laser parameters, a complete laser surface melting (LSM) or a selective laser surface melting (SLSM) were reached. The microstructure, mechanical properties and corrosion behaviour were established and compared. Higher laser input energies led to larger treated zones and in these cases two different regions could be distinguished: the outer zone, where the LSM took place, presented a more refined microstructure with a greater dispersion of secondary phases; the following zone suffered SLSM, in it only the secondary phases were modified by the HPDL. Hardness was 24 % – 27 % higher than that of the untreated samples. The HPDL also reduced the corrosion rate by 21 % and 37 % for the Mg-1Zn-1Ca alloy and the Mg-3Zn-0.4Ca alloy, respectively, after 336 h of immersion in Hanks' solution at 37 °C.

Keywords

Laser treatment; High Power Diode Laser; Magnesium alloys; Corrosion; Biodegradable implants; Biomaterials;

1. Introduction

For the development of biodegradable implants, materials with mechanical properties close to those of the bone are preferable. Mg and its alloys are considered potential candidates for this application since they present low density (1.74 g cm^{-3}) and an elastic modulus from 41 to 45 GPa, showing high specific resistance values. However, the use of Mg and its alloys is limited due to their high degradation rate. For this reason, most of the studies on Mg are focused in the improvement of their corrosion resistance.

There are different ways to protect Mg and its alloys against corrosion, among them, the most studied ones are the deposition of protective coatings, alloying and the modification of the microstructure. Plasma electrolytic oxidation (PEO) [1], sol-gel [2] and hydrothermal process [3] are some of the techniques found to improve the corrosion behaviour of the Mg and its alloys by the deposition of a protective coating. Y. Ding et al. [4], K. Gusieva et al. [5] and M. Esmaily et al. [6] have studied the effect of different alloying elements on the corrosion performance of Mg and its alloys. Among the alloying elements, Ca and Zn are suitable for biomedical applications because of their natural presence in the human body and the vital functions carried out by them in the organism. These alloying elements increase the hardness of the alloy by forming the Mg_2Ca and $Ca_2Mg_6Zn_3$ precipitate phases [7]. However, they also cause galvanic

corrosion because of the galvanic couple formed between the α-Mg phase and the precipitated phases [8,9].

The role of the microstructure on the corrosion behaviour of the Mg-based alloys has been studied by using different ageing treatments [10,11] and different production process such as casting or wrought [12,13]. Another alternative method proposed to produce microstructural changes on Mg and its alloys are the laser surface treatments. Depending on the applied laser input energy, two different types of surface modifications can be obtained: high input laser energies produce the laser surface melting (LSM), while lower input laser energies lead to selective laser surface melting (SLSM). These techniques stand out due to the high precision offered by the laser beams and the very localized thermal action produced. The modification of the surface properties by the LSM process is based on the rapid melting of a thin layer on metal surface followed by rapid solidification (cooling rates in the order of 10^5 to 10^8 K/s). LSM can form a homogeneous and refined microstructure, reduce the microsegregation, dissolution and redistribution of precipitates or inclusions, transform the phases of the alloys and increase solid solubility. After LSM, the microstructure dependent properties, such as hardness, wear and corrosion resistance are improved [14]. The SLSM process allows the melting of one or more phases of the alloy, while keeping unaltered the other phases that constitute the material. This prevents problems derived from the secondary phases, such as fragility, low fatigue resistance and low wear behaviour caused by brittle phases, and increases the corrosion resistance by reducing galvanic couples in the alloys [15]. The High Power Diode Laser (HPDL) technology can produce an uniform heating on the surface on a relatively large area, leading to the homogenization and refinement of the

microstructure and the dissolution of the secondary phases. Moreover, compared to other laser sources (CO_2, Nd:YAG and excimer lasers), HPDLs present some advantages such as ease of integration due to its small size and low weight, low running costs because of its high efficiency and reliability, reduced maintenance and energy consumption and long lifetime [16,17]. J. Rams et al. [16] employed a HPDL to produce the laser surface melting of aluminium matrix composites reinforced with SiC particles. The melted layer showed a more homogenized and refined microstructure, which led to composites with increased corrosion resistance and surface hardness. In a subsequent study, F. Viejo et al. [18] used a HPDL to improve the corrosion resistance of aluminium composites by laser surface melting. They also observed a refined microstructure with homogeneous microdendrites and absence of cathodic intermetallic compounds in the laser-treated region, which improved the surface hardness and reduced the localised corrosion.

C. Taltavull et al. [19–22] conducted a deep study of the influence of the HPDL on the corrosion behaviour and mechanical properties on an AZ91D alloy. At high input laser energies, the complete LSM occurred, while using lower input laser energies, SLSM took place and only the β-phase ($Mg_{17}Al_{12}$) was molten, leaving the other phases untreated. After the complete laser surface melting, the hardness in the treated zone significantly increased compared to the as-cast AZ91D alloy. However, when the SLSM process was performed, the β-phase reduced its hardness and the hardness of the α-Mg matrix kept almost unaltered. They also observed that the SLSM of the secondary phase produced an increase of 40 % of the fracture toughness of the AZ91D alloy because of the transition from brittle to ductile fracture behaviour of the β-phase that constituted the crack initiator. Finally, regarding the corrosion behaviour, they

concluded that the SLSM treatments led to lower corrosion rates than in the AZ91D alloy. For the LSM treatments the corrosion rate was found to be higher due to several factors such as surface deformation, residual stress and existence of voids in the surface, which had more effect on the corrosion behaviour than the microstructural modifications introduced by the laser treatment. Nevertheless, after removing the most external laser-treated samples, they achieved a reduction in the corrosion rate of the LSM samples.

Furthermore, Y. C. Guan et al. [23], B. Manne et al. [24] and K. R. Rakesh et al. [25] demonstrated the effectiveness of the LSM on the corrosion improvement of AZ91D alloy, Mg-Zn alloy and Mg-Zn-Dy alloy, respectively, for biodegradable implant applications. In the first study, the general and pitting corrosion in a simulated body fluid were improved because of the formation of a refined continuous network of β-phase ($Mg_{17}Al_{12}$) and the increase of the Al concentration in the laser-treated zones. In the second work, the corrosion rates were highly reduced because of the microstructural refinement and homogenization and the Zn enrichment of the matrix caused by the LSM. Finally, in the third study, a higher homogenisation and grain refinement in the LSM region was observed due to the rapid heating and cooling cycle. The LSM also induced surface roughness, enhancing the wettability of the Mg-Zn-Dy alloy. The corrosion rate in Hanks' Balanced Salt Solution (HBSS) decreased in the laser-treated samples. C. Ma et al. [26] and J. Zhang et al. [27] also enhanced the mechanical properties, corrosion resistance and biocompatibility of Mg-Gd-Ca alloy by laser surface processing. They showed the effectiveness of laser treatment to control cell behaviour. Additional research related to the use of laser treatments for biomedical applications can be found in bibliography [28–30].

In the current study, two Mg-Zn-Ca alloys have been laser-treated using a HPDL in order to modify their microstructure to improve mechanical properties and corrosion behaviour to use them in biomedical applications. For it, different laser parameters have been applied to obtain microstructures that cannot be obtained by a conventional casting process and to get an alloy with a more homogeneous composition and distribution of secondary phases. The microstructures obtained have been studied, the properties of the modified materials have been tested by hydrogen evolution, electrochemical impedance spectroscopy (EIS) and a correlation between microstructure and properties has been derived.

2. Materials and Methods

2.1. Materials

The as-cast Mg-1Zn-1Ca and Mg-3Zn-0.4Ca alloys were supplied by the Helmholtz Zentrum Geesthacht (Germany). The chemical composition of the alloys, analysed by spark emission spectroscopy and atomic absorption spectrometry, is listed in Table 1.

Table 1. Compositional analysis of the as-cast Mg-1Zn-1Ca and Mg-3Zn-0.4Ca alloys.

Element (wt. %)	Ca	Zn	Fe	Cu	Ni	Mg
Mg-1Zn-1Ca	1.47	1.01	0.0071	0.0015	0.0007	Bal.
Mg-3Zn-0.4Ca	0.40	3.14	0.0120	0.0015	0.0008	Bal.

2.2. Laser Surface Treatment

Samples were painted with a black topcoat based on acrylic resin to improve the absorption of the laser radiation and to avoid the oxidation of the samples during

the laser treatment. Then, specimens were superficially treated by using a continuous wave High Power Diode Laser (HPDL) Rofin DL013S with a maximum power of 1300 W and an emission wavelength of 808 – 940 nm, controlled by an ABB IRB 2400/16 robot. The laser power and the laser scanning speed were controlled. After laser treatment, the paint on the surfaces was removed using isopropanol. Finally, specimens were ground with 1200 grit SiC paper, cleaned in an ultrasonic bath for 5 min and dried using hot air.

Table 2 shows the laser power, the laser scanning speed and the laser input energy for each condition used through this work. Previously, more and less energetic conditions were studied and discarded due to full melting of the samples, which caused new microstructures with defects, or because the laser had no effect in the alloy, respectively. The heat input (*HI*), i.e., energy per unit length was calculated using Eq. 1 [31]:

$$HI = \frac{P}{v} \qquad \text{Eq. 1}$$

Where *P* is the laser power and *v* is the scanning velocity.

Table 2. Laser treatment parameters.

Laser power (W)	743	743	743	743
Scanning speed (mm s^{-1})	75	80	85	90
Heat input (10^{-3} J m^{-1})	9.9	9.3	8.7	8.3

Samples with dimensions 30 x 2.5 x 2.5 mm^3 were used to study the microstructure, the volume of hydrogen evolved and the microhardness of the alloys. These dimensions were selected to optimize the parameters according to the real

dimensions of the implants for rabbit femurs. The laser procedure used for these specimens is shown in Figure 1a. Firstly, the power and the scanning speed of the laser treatment are selected. Then, a laser pass is performed on each lateral face of the sample maintaining the same laser conditions. For the electrochemical impedance spectroscopy (EIS) tests, samples with dimensions 30 x 25 x 2.5 mm^3 were used, so they could be tested in normalized cells. When the power and the scanning speed of the laser treatment are selected, the laser traces a path on one of the surfaces of the specimens (Figure 1b) with a spacing of 1.5 mm between consecutive scans with an overlap of 30 %. The distance between the laser and the surface of the specimens was 9 mm for all samples. In both cases, a preheating is carried out on the surface where the sample is placed for laser treatment.

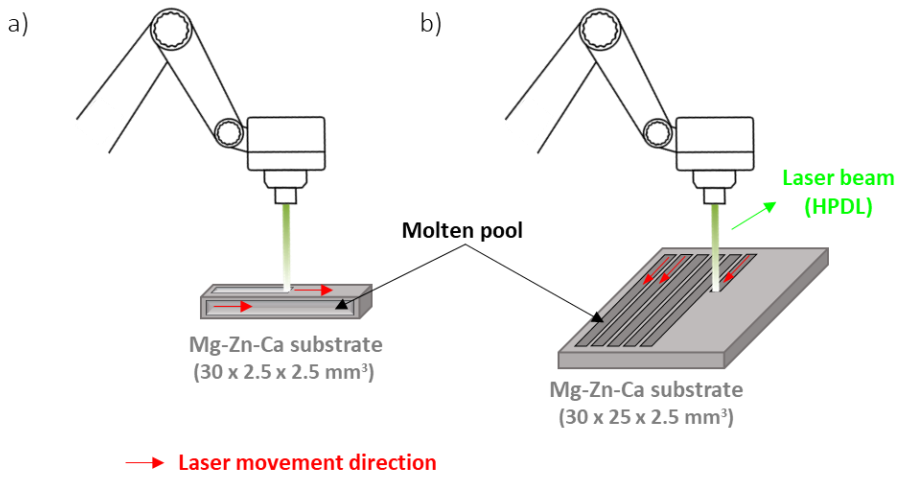

Figure 1. a) Laser treatment for samples of dimensions 30 x 2.5 x 2.5 mm^3; b) Laser treatment for samples of dimensions 30 x 25 x 2.5 mm^3.

2.3. Microstructural Characterization

A Scanning Electron Microscope (SEM, Hitachi S-3400N) equipped with an Energy Dispersive X-Ray Spectrometer (EDS, Bruker AXS Xflash Detector 5010) was

used to analyse the microstructural changes on the samples after laser treatment and to observe the corrosion progress. For it, samples were cross-cut, embedded in conductive resin, mechanically polished (up to 1 μm) and etched in Nital solution (2 vol. % nitric acid and 98 vol. % ethanol) to reveal the microstructure.

2.4. Mechanical Characterization

The microhardness of the Mg-Zn-Ca alloys was determined using a Microhardness Tester (SHIMADZU HMV-2TE) with applied loads of 980.7 mN ($HV_{0.1}$) for 20 s. Samples were mechanically polished with diamond paste up to 1 μm. The average value was calculated after ten indentations.

2.5. Hydrogen evolution test

The experimental set up used in this test was described by Shi et al [32]. Samples of dimensions 30 x 2.5 x 2.5 mm^3, in the as-received and laser-treated conditions, were ground with 1200 grit SiC paper. After that, specimens were immersed in Hanks' solution. The temperature and pH of the solution were monitored, and they remained steady throughout the test. The temperature was kept at 37 °C using a thermostatic bath and carbon dioxide (CO_2) was bubbled through the solution to maintain a constant pH value of 7.4. Corrosion rate, P_H (mm y^{-1}), was determined by the hydrogen evolution rate measured after 336 hours of immersion, using the Eq. 2 [32]:

$$P_H = 2.279\ V_H \qquad \text{Eq. 2}$$

2.6. Electrochemical Impedance Spectroscopy (EIS)

EIS electrochemical measurements were carried out using a Gamry Interface 1000 potentiostat inside a Faraday cage. A conventional three-electrode cell was used with a silver/silver chloride reference electrode (Ag/AgCl), a platinum foil counter electrode and the studied sample as the working electrode, with an exposed area of 0.5 cm^2. The measurements were performed at different immersion times: 1, 2, 4, 24 and 48 h in Hanks' solution at room temperature. For it, a sinusoidal potential was applied at the open circuit potential (*OCP*) with an amplitude of 10 mV RMS over the frequency range from 10^5 to 10^{-2} Hz, recording 9 points per frequency decade. The EIS data were fitted to an equivalent circuit using the Gamry Echem Analyst software.

3. Results and Discussion

3.1. Microstructural Characterization

The microstructure of the as-received Mg-1Zn-1Ca and Mg-3Zn-0.4Ca alloys is shown in Figure 2. The as-cast Mg-1Zn-1Ca alloy presents a continuous network of secondary phases (Figure 2a) that consists of Mg_2Ca and $Ca_2Mg_6Zn_3$, as observed in Figure 2b. In it, the $Ca_2Mg_6Zn_3$ phase is surrounding the Mg_2Ca phase and it is preventing the formation of galvanic couples between the Mg_2Ca particles and the α-Mg matrix. The EDS mapping of the analysed zone indicates that Ca and Zn are mainly located at the grain boundaries forming the intermetallic compounds and the α-Mg matrix is constituted basically by Mg. As observed in the as-cast Mg-3Zn-0.4Ca alloy microstructure (Figure 2c), a secondary phase has precipitated at the grain boundaries, at the triple junctions and within the grains. The precipitated particles (Figure 2d) show a eutectic morphology. As the $Ca_2Mg_6Zn_3$ phase is nobler than the α-Mg matrix [9], the

corrosion progresses through this one. From the EDS mapping of the studied zone it is possible to stablish that the α-Mg matrix is mainly constituted by Mg and the precipitates correspond to the intermetallic compound $Ca_2Mg_6Zn_3$. Further information related to these alloys can be found in previous studies available in literature [33,34].

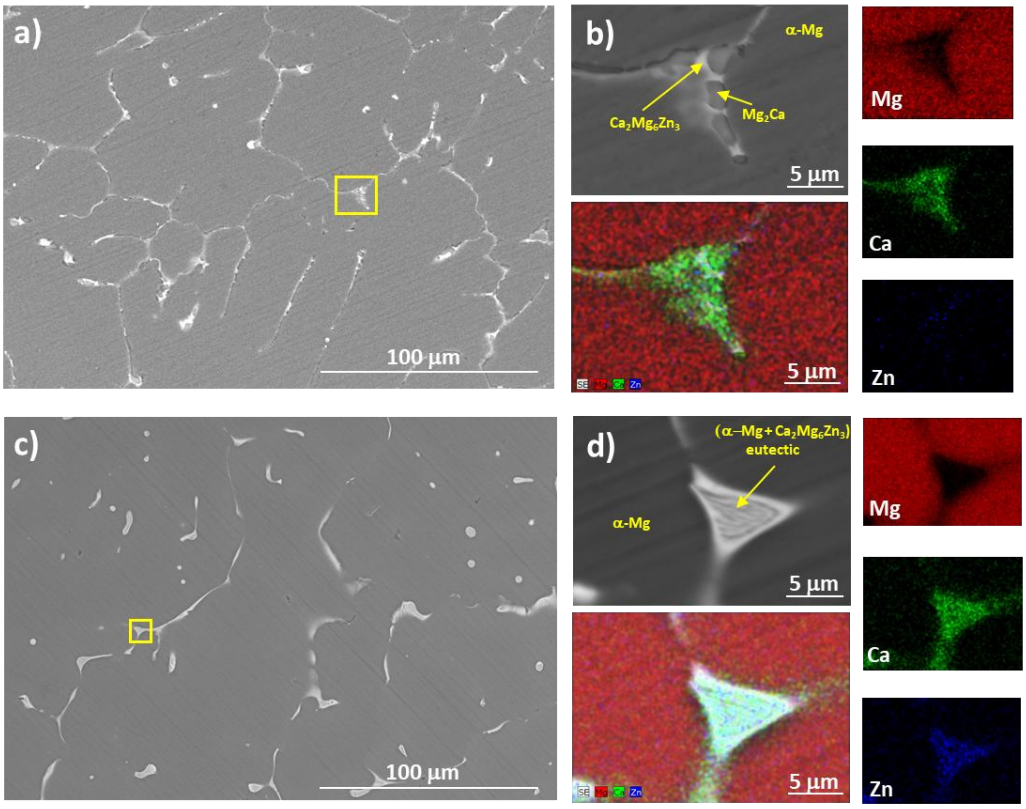

Figure 2. SEM-BSE images of as-received (a) Mg-1Zn-1Ca and (c) Mg-3Zn-0.4Ca alloys. Constituents and EDS mapping analysis of the selected area for b) Mg-1Zn-1Ca and d) Mg-3Zn-0.4Ca alloys showing the distribution of the Mg, Ca and Zn elements.

HPDL treatments produced changes in the microstructure of the studied Mg-Zn-Ca alloys. Figure 3a, related to the 80 mm s^{-1} laser-treated Mg-1Zn-1Ca alloy, shows in detail the different zones that can be differentiated in the resulting microstructure. The first zone (Z1) corresponds to the outer zone of the sample, where

the complete LSM of the sample surface occurred. In this zone the temperature was above the melting points of all the phases present in the alloy, i.e., the α-Mg matrix and the Mg_2Ca and $Ca_6Mg_2Zn_3$ secondary phases were fully melted. The fast solidification afterwards is responsible of the formation of a much more refined and homogeneous microstructure than in the as-received condition (Figure 2a). Figure 3b represents a magnification of the microstructure in Z1. As observed, the secondary phases are more refined, and they are not forming a continuous network through the sample. At this point, it is also noticeable that the Mg_2Ca phase is more exposed as it is not embraced by the $Ca_2Mg_6Zn_3$ phase.

At the laser-treated zone Z2, the SLSM of the secondary phases happened. In this zone, the temperature reached by the sample because of the laser treatment is lower than in Z1, being below the melting point of the α-Mg matrix. This causes that only the intermetallic compounds that present low eutectic melting points are molten. In this zone, the microstructure of the secondary phases is modified without apparently modifying the α-Mg matrix. Figure 3c shows a magnification of one of the secondary phases found in Z2. Its main observable feature is that it is thicker than in the untreated case. This suggests that the intermetallic precipitate was melted, while the surrounding α-Mg matrix remained solid. However, the molten material was capable of dissolving some of the matrix around, increasing the amount of molten material. Then, after the laser pass, the molten material solidifies, but its composition does no longer correspond to that of the intermetallic precipitated as it is enriched in Mg. So, it solidifies with a eutectic structure. It is also noticeable an enrichment in Zn of the α-Mg matrix. It could be related to the rapid solidification, which could produce

an increase in the solid solubility of Zn into the matrix [35]. Below the Z2 zone, the microstructure corresponds to the bulk material, where the HPDL had no effect.

In the non-treated zone, there was no melting of any of the phases of the microstructure. Any change in it should have taken place in solid state, but its microstructure was identical to that of the substrate before the laser treatment.

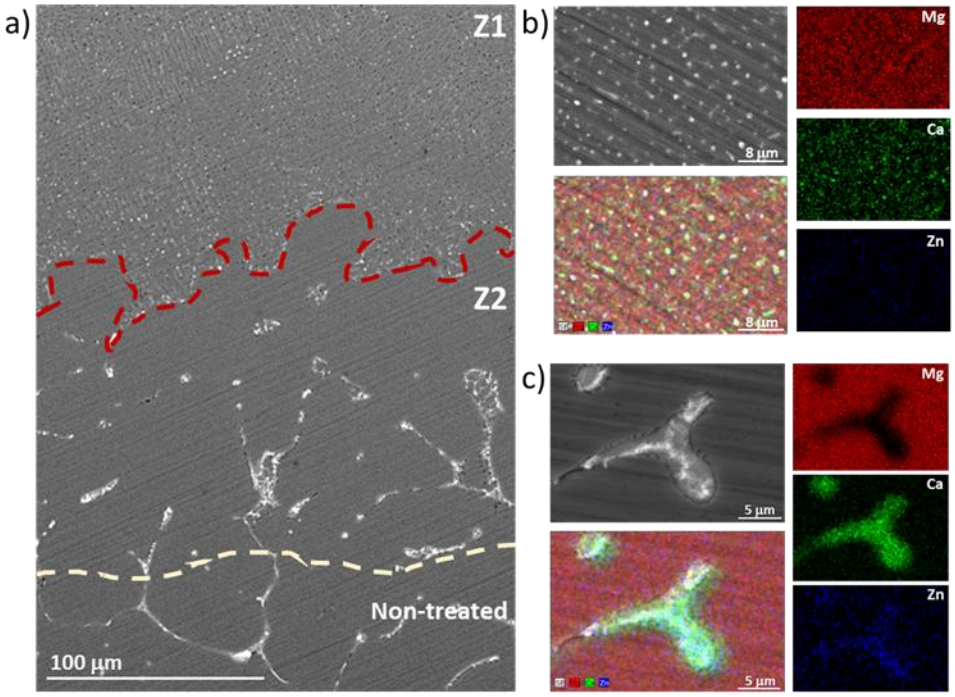

Figure 3. a) SEM-BSE image of a cross-section of the 80 mm s^{-1} laser-treated Mg-1Zn-1Ca alloy sample showing zones with different microstructure: the laser-treated zones (Z1 and Z2) and the non-treated region. SEM-BSE image and EDS mapping of b) precipitates in Z1 and c) a precipitate found in Z2.

The microstructure observations for the 80 mm s^{-1} laser-treated Mg-3Zn-0.4Ca alloy are shown in Figure 4a, where three zones with different microstructure, marked as Z1, Z2 and non-treated, can be observed. The laser

parameters selected produced a complete LSM in the outer zone (Z1) where the secondary phases were homogeneously and finely precipitated after cooling (Figure 4b). At the intermediate zone (Z2), only the $Ca_2Mg_6Zn_3$ intermetallic compounds were selectively molten as they present a lower melting point than the α-Mg phase. After laser treatment, the microstructure of these secondary phases was much more refined, although the eutectic structure was preserved, as observed in Figure 4c. The area below is related to that of the microstructure that does not suffer any change on it, so it corresponds to the bulk material.

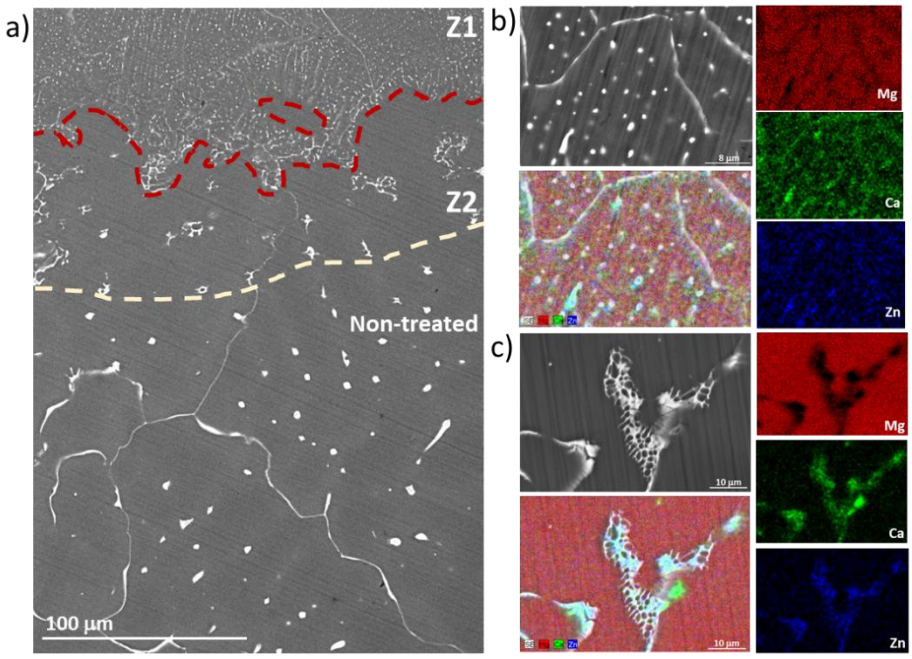

Figure 4. a) SEM-BSE image of a cross-section of the 80 mm s^{-1} laser-treated Mg-3Zn-0.4Ca alloy sample showing zones with different microstructure: the laser-treated zones (Z1 and Z2) and the non-treated region. SEM-BSE image and EDS mapping of b) precipitates in Z1 and c) a precipitate found in Z2.

The microstructural modifications depended on the laser input energy, as shown in Figure 5, where red arrows define the complete laser surface melting (LSM)

of the sample and yellow arrows determine the selective laser surface melting (SLSM) suffered only by the secondary phases. Higher laser input energies caused a deeper LSM followed by a deeper SLSM, that is, the depth of the overall laser treatment is greater than in the laser-treated samples using lower input energies. No substantial differences between the molten zones in the different samples were found. It is also observable the different modifications suffered by both Mg-Zn-Ca alloys. Providing the same laser input energies, the Mg-1Zn-1Ca alloy registered greater microstructural changes compared to the Mg-3Zn-0.4Ca alloy. These differences can be ascribed to the secondary phases presented in each alloy, whose melting point is as follows: $Ca_2Mg_6Zn_3$ (390 °C – 420 °C) < Mg_2Ca (490 °C - 520 °C) < α-Mg (650 °C) [8,36–39]. For both alloys, depths of these regions depend on the laser input energy. In both cases, using 90 mm s^{-1} of laser scanning speed, makes that only the SLSM of the intermetallic compounds was observed. After the laser treatments, no oxidation was detected on the treated surfaces.

The treatment in the Mg-1Zn-1Ca alloy was deeper than in the Mg-3Zn-0.4Ca alloy, indicating a higher thermal conductivity of the former alloy. Thermal conductivity is influenced by the conductivity of the phases present in the alloy and by their spatial distribution.

In the α-Mg phase, conductivity is enhanced by reducing the number of dissolved atoms. From references [33,34] it is known that the studied Mg-1Zn-1Ca alloy presents lower amounts of alloying elements diluted in the matrix than the Mg-3Zn-0.4Ca alloy, favouring the thermal conductivity of the former one. It has been

observed that the thermal conductivity of precipitated phases increases with the speed of sound in them, which is high for the MgZn [40]. Also, they are more abundant in the Mg-1Zn-1Ca alloy, favouring the thermal conductivity of this alloy. Finally, the distribution of phases is different in both cases. The Mg-1Zn-1Ca shows a net-like continuous phase at grain boundaries, while the Mg-3Zn-0.4Ca shows distributed phases. In AZ91D magnesium alloys [41] and in Mg alloys containing W-phase [42,43], the existence of a net-like continuous phase has been correlated with high thermal conductivity because precipitation consumes the solute elements in the matrix and the continuity of the phase at the grain boundary, both promoting long-distance movement of phonons, thereby improving the thermal properties. Also, the images of the microstructure of the Mg-1Zn-1Ca laser-treated samples indicate that most transformations take place around the precipitated phase, suggesting that it may have had a strong effect in heat transport from the surface to the interior of the materials. On the other hand, in the Mg-3Zn-0.4Ca alloy the phase distribution acts as a disturbance for the movement of phonons, hence reducing heat transport to the interior of the samples.

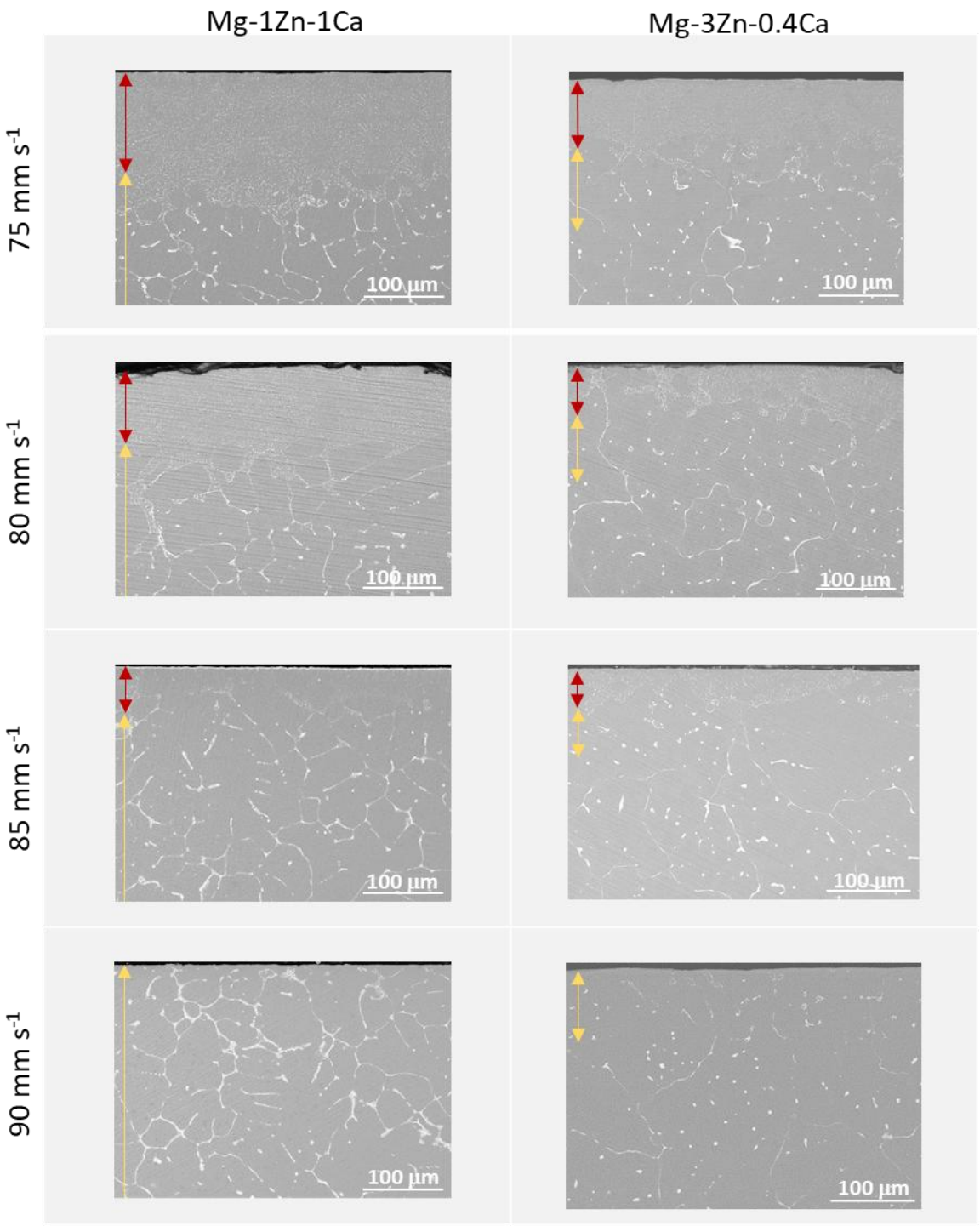

Figure 5. SEM-BSE images of laser-treated samples applying different laser input energies. Red arrows indicate complete laser surface melting (LSM) and yellow arrows indicate selective laser surface melting (SLSM).

3.2. Hardness measurements

After the laser treatment, the microhardness at the outer zone of the samples was measured. Results are shown in Figure 6. For both alloys, Mg-1Zn-1Ca and Mg-3Zn-0.4Ca, the laser-treated samples present higher hardness values than the as-received ones. The increase of hardness in the Mg-1Zn-1Ca alloy ranged from 13 to 24 %, while for the Mg-3Zn-0.4Ca it was comprised between 11 % and 27 %, depending on the laser parameters. It indicates that there was a significant hardening effect by the HPDL treatment on the alloys because of the rapid cooling suffered by the laser-treated samples.

Generally, the faster the treatment, the greater the hardness, as expected from a higher cooling speed. The excess of heat that the LSM provides causes a slower cooling of the surface of the samples and hardness is smaller. In the SLSM treatment, the small molten volume has a low heat capacity and the cooling is much faster, causing higher hardness values.

The highest hardness increase was achieved using the 85 mm s^{-1} laser scanning condition in both alloys. The heating and subsequent rapid cooling caused in that condition produced modification in the size and shape of the intermetallic precipitates, and the formation of thicker eutectic structures. From these results it is possible to establish that the complete melting of the samples in LSM treatments does not lead to the higher hardness values. The SLSM of the secondary phases is enough to produce microstructures with higher hardness values. Despite this, the microstructure of each zone is similar to the one obtained with other treatments, but the transformed volume is balanced to provide maximum surface properties.

At 90 mm s^{-1}, the treatment suffered by the sample was lower as less volume of material was affected. In this case, microhardness tests measured both, treated and untreated zones, resulting in lower hardness values despite the presence of SLSM.

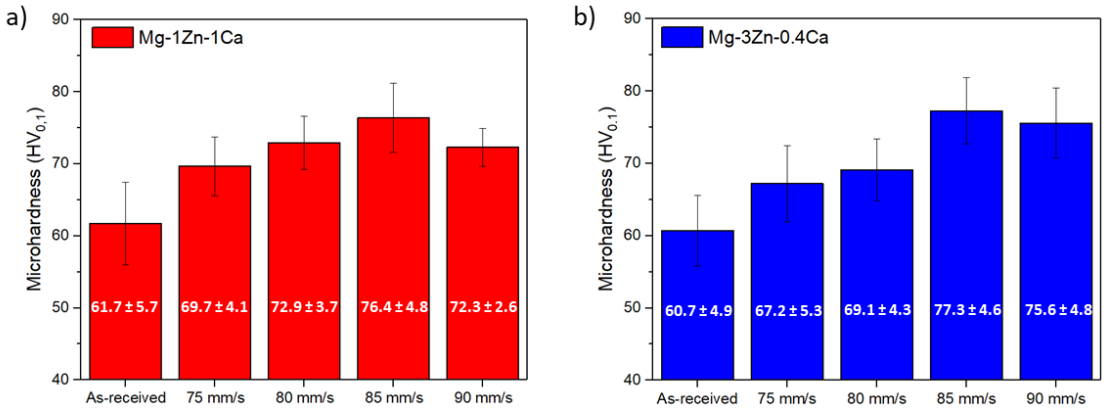

Figure 6. Microhardness evolution with laser treatment for a) Mg-1Zn-1Ca alloy and b) Mg-3Zn-0.4Ca alloy. 75, 80, 85 and 90 are referred to the laser scanning speed in mm s^{-1}.

3.3. Immersion tests

The hydrogen evolution of the as-received and laser-treated Mg-1Zn-1Ca and Mg-3Zn-0.4Ca alloys after 336 of immersion in Hanks' solution at 37 °C is recorded in Figure 7. As observed, the volume of evolved hydrogen increases with immersion time in Hanks' solution and two different tendencies in the corrosion behaviour could be distinguished for each condition. Eq. 2 was used to obtain the corrosion rate (P_H) of both Mg-Zn-Ca alloys at the two different intervals. Table 3 and Table 4 present the corresponding P_H values obtained for the Mg-1Zn-1Ca and the Mg-3Zn-0.4Ca alloys, respectively.

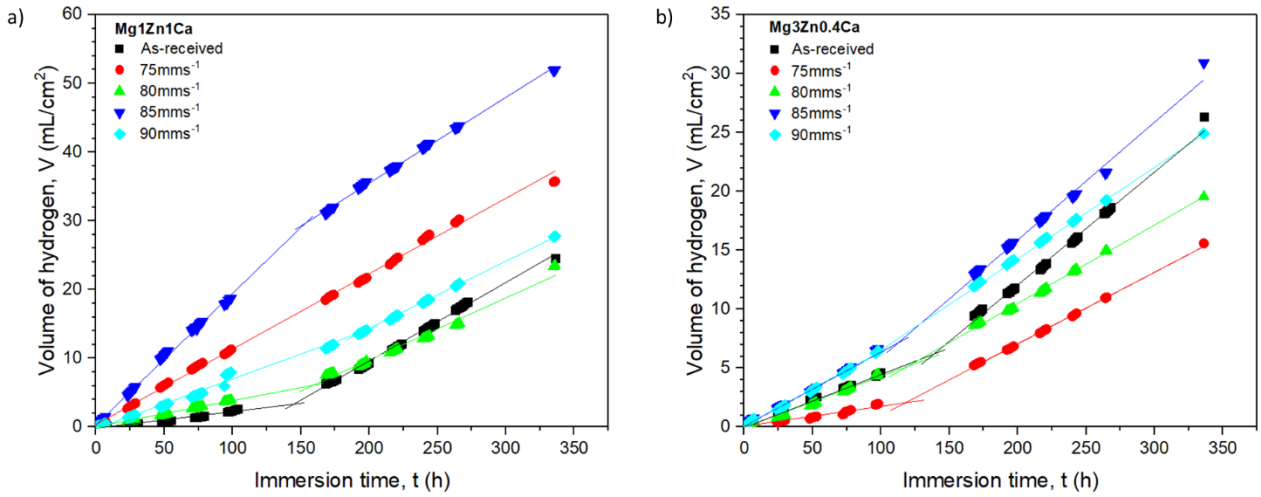

Figure 7. Hydrogen evolution data after 336 h of immersion in Hanks' solution at 37 °C for a) as-received and laser-treated Mg-1Zn-1Ca alloy and b) as-received and laser-treated Mg-3Zn0.4Ca alloy.

Table 3. Corrosion rate (P_H) for the Mg-1Zn-1Ca alloy for samples of dimensions: 30 x 2.5 x 2.5 mm^3.

Mg-1Zn-1Ca alloy				
Condition	***Time interval 1 (in hours)***	***P_{H1} (in mm y^{-1})***	***Time Interval 2 (in hours)***	***P_{H2} (in mm y^{-1})***
As-received	0 - 145	1.29	145 - 336	6.25
75 mm s^{-1}	0 - 336	6.00	0 - 336	6.00
80 mm s^{-1}	0 - 161	2.09	161 - 336	4.94
85 mm s^{-1}	0 - 155	10.41	155 - 336	6.82
90 mm s^{-1}	0 - 198	3.98	198 - 336	5.32

Table 4. Corrosion rate (P_H) for the Mg-3Zn-0.4Ca alloy for samples of dimensions: 30 x 2.5 x 2.5 mm^3.

Mg-3Zn-0.4Ca alloy				
Condition	***Time interval 1 (in hours)***	***P_{H1} (in mm y^{-1})***	***Time interval 2 (in hours)***	***P_{H2} (in mm y^{-1})***
As-received	0 – 129	2.19	129 - 336	5.23
75 mm s^{-1}	0 – 118	0.94	118 - 336	3.32
80 mm s^{-1}	0 – 115	2.37	115 - 336	3.60
85 mm s^{-1}	0 - 114	3.47	114 - 336	5.44
90 mm s^{-1}	0 - 72	3.45	72 - 336	4.19

For the as-received conditions, the first time interval is associated with a general corrosion mechanism suffered by the Mg-1Zn-1Ca and Mg-3Zn-0.4Ca alloys. At the second time interval, localized corrosion is the dominant corrosion mechanism in these alloys, as it is shown in the literature [33]. Moreover, the volume of hydrogen gas evolved by the studied Mg-1Zn-1Ca and Mg-3Zn-0.4Ca alloys is lower than that released by other Mg-based alloys containing Zn, Ca, Mn, Ce and Al [44–47].

For the laser-treated conditions other aspects must be considered when determining the differences in the slopes obtained for the two different time intervals. The HPDL produces modifications in the microstructure and, therefore, it is expected that different microstructures present different corrosion rates. The corrosion progression could be different in the LSM zone, the SLSM region and the bulk material. The galvanic couple formed in each zone between the α-Mg and the secondary precipitated phases after the rapid cooling will determine the corrosion rate of the resulting alloy. For the Mg-1Zn-1Ca alloy, after laser treatment, the $Ca_2Mg_6Zn_3$ intermetallic compound does not appear always embracing the Mg_2Ca secondary phase which implies a higher exposition of the Mg_2Ca, more active than the $Ca_2Mg_6Zn_3$

phase. This is different from what is observed in the untreated alloy. In it, the $Ca_2Mg_6Zn_3$ phase is embracing the Mg_2Ca one, so the galvanic couples are formed between the α-Mg matrix and the $Ca_2Mg_6Zn_3$ phase, instead of forming it with the more anodic phase, Mg_2Ca. For this reason, in the untreated alloy the corrosion takes place through the α-Mg matrix without attack to the secondary phases, which act as barriers against corrosion. In terms of corrosion, this change implies, in general, higher corrosion rates compared to the as-received Mg-1Zn-1Ca alloy in the first time interval. Nevertheless, in the second time interval, the corrosion rates decreased in some conditions, reaching a 21 % of reduction in the 80 mm s^{-1} condition. For the Mg-3Zn-0.4Ca alloy, the HPDL effect is more significant on the corrosion rates. The precipitates formed after laser treatment present an enrichment in Mg, which leads to a smaller galvanic couple formed between the α-Mg and the precipitated secondary phase. For this reason, a better corrosion performance is reached for this alloy. The corrosion rate was reduced by up to 37 % in this alloy. These results show the effectiveness of the HPDL in reducing the corrosion rate of the Mg-Zn-Ca alloys. Controlling the corrosion rate is also essential for materials to be used in biodegradable implants.

In both alloys, the condition that presented the higher microhardness value, i.e. 85 mm s^{-1}, shows the superior value of hydrogen evolved. Higher hardness values are related to higher amounts of residual stresses and this can be the cause of their higher corrosion rates.

Finally, comparing both alloys, it can be seen that the Mg-3Zn-0.4Ca alloy presents a better corrosion behaviour than the Mg-1Zn-1Ca alloy, in as-received

conditions and after different laser treatments. As shown in Figure 7, the volume of hydrogen released by the Mg-1Zn-1Ca alloy is higher than in the Mg-3Zn-0.4Ca in most conditions and at the two different time intervals.

The corrosion progress of the Mg-1Zn-1Ca alloy is shown in Figure 8. As referred before, in the as-received Mg-1Zn-1Ca alloy, the $Ca_2Mg_6Zn_3$ phase is embracing the more anodic Mg_2Ca phase. For this reason, the corrosion advances through the α-Mg matrix and the secondary phases act as local barriers against corrosion progression (Figure 8a). After the laser treatment, the two different phases precipitate separately and the galvanic couple formed between the Mg_2Ca phase and the α-Mg matrix promotes the corrosion of the more anodic phase, i.e., the Mg_2Ca phase, as shown in Figure 8b. The $Ca_2Mg_6Zn_3$ phase, which is the noblest phase in the alloy, remains uncorroded.

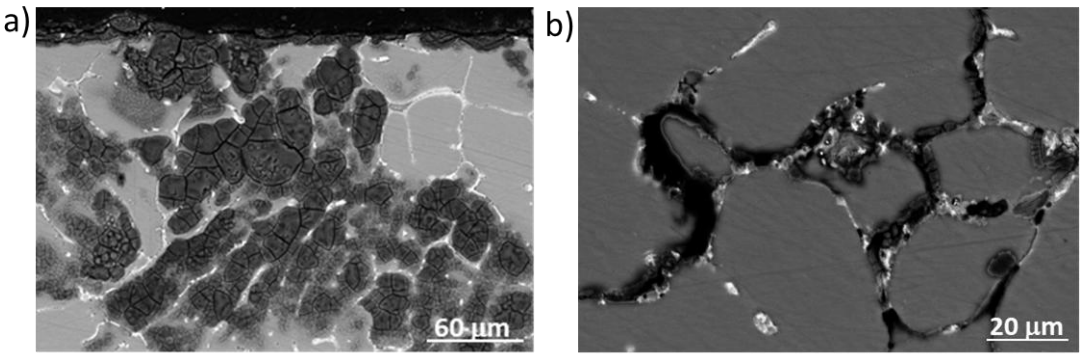

Figure 8. Corrosion progression in the cross-section of: a) as-received Mg-1Zn-1Ca alloy and b) 90 mm s^{-1} laser-treated Mg-1Zn-1Ca alloy.

As shown in Figure 9, for the Mg-3Zn-0.4Ca alloy the corrosion progression took place through the α-Mg matrix regardless of whether the sample was in the as-received state or in a laser-treated condition. It is due to the more anodic character of the

α-Mg phase compared to the $Ca_2Mg_6Zn_3$ phase, which remains unaffected by the corrosion. When the microstructure is refined (Figure 9b), the precipitates act as local barriers hampering the corrosion progression, which is forced to advance between the precipitated phases.

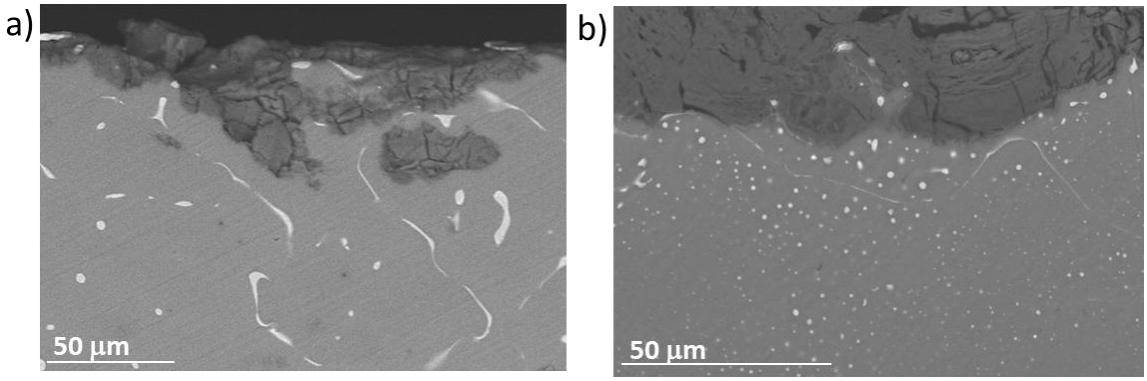

Figure 9. Corrosion progression in the cross-section of: a) as-received Mg-3Zn-0.4Ca alloy and b) 80 mm s^{-1} laser-treated Mg-3Zn-0.4Ca alloy.

3.4. Electrochemical Impedance Spectroscopy (EIS)

Figures 10 and 11 display Nyquist and Bode plots of the EIS measurements for the as-received Mg-1Zn-1Ca and Mg-3Zn-0.4Ca alloys and the same alloys after laser treatment using a laser power of 743 W and different laser scanning speeds (75 mm s^{-1}, 80 mm s^{-1}, 85 mm s^{-1} and 90 mm s^{-1}), up to 48 h of immersion in Hanks' solution at room temperature.

According to Figure 10, the laser-treated conditions do not improve the corrosion performance of the as-received Mg-1Zn-1Ca alloy. Only the 90 mm s^{-1} condition shows values closer to those of the as-received one. In Figure 11 it is possible to observe that the 75 mm s^{-1}, 85 mm s^{-1} and 90 mm s^{-1} laser-treated samples present a higher modulus of impedance in a wide frequency range than the as-received Mg-3Zn-0.4Ca alloy after different immersion periods. Moreover, the 80 mm s^{-1} laser-

treated condition shows similar values to this one. The effectiveness of the HPDL treatment is superior in the Mg-3Zn-0.4Ca alloy than in the Mg-1Zn-1Ca alloy. This result agrees with the one obtained from the hydrogen evolution test at longer immersion times. Another consequence derived from the laser treatment is the growing instability of the system when the most energetic conditions are used. The treated samples generally tend to demonstrate more signs of non-stationarity during immersion, especially in the initial period. The non-stationarity is evidenced from the scattering of data points at lower frequencies and clearly evident pseudo-inductive behaviour. The pseudo-inductance at low frequencies in Mg-based systems very often appears as a result of activation of the corrosion processes during the acquisition of a spectrum, when going to frequency range below 1 Hz [48].

A relaxation process can be observed at frequencies ranging from 10^1 – 10^2 Hz, which is related to the response from the nanoscale MgO film present on the Mg substrate when it is immersed in an aqueous media. Moreover, an additional relaxation process can be observed at high frequencies (10^3 – 10^4 Hz), in the as-received state and in the laser-treated conditions, when samples are immersed in Hanks' solution. This time constant, which grows with immersion time, is related to the formation of an additional semi-protective layer on top of the $MgO/Mg(OH)_2$ layer previously cited due to the presence of the Ca^{2+}, HPO_4^{2-} and HCO_3^- ions in the electrolyte [49,50].

Figure 12 shows the equivalent circuit used to fit the experimental data. R_e is the electrolyte resistance, R_{f1} and CPE_{f1} are introduced because of the formation of the

partially protective layer on top of the MgO/$Mg(OH)_2$ layer. R_{f2} and CPE_{f2} correspond to resistance and capacitance of MgO film, respectively. At low frequencies, at which the electrochemical reactions on the surface are manifested, most of Mg systems did not maintain stationary conditions as can be seen from the scattering of data points and pseudo-inductive behaviour. Therefore, this spectra region was discarded to perform the fittings and the respective elements are not present in the suggested equivalent circuit. The equivalent circuit with two time constants was used here to fit the spectra within a limited higher frequency range, which is not affected by the non-stationarity. It is important to mention that the corrosion processes are not absent on the surface in those cases. However, they are impossible to properly fit since the corrosion current density evolves during the spectra acquisition resulting in inductive loops and data point scattering. The time constant associated to the electrochemical activity can be seen for example on untreated surfaces at about 0.1 Hz. Nevertheless, even in those cases its proper quantification is rather complicated considering a very low charge transfer resistance at corroding Mg interface. Therefore, the EIS analysis in the present work was only limited to assess evolution with time of two important components, namely the resistance of the protective MgO layer at the surface and the resistance of the newly precipitated layer on top. These EIS fitting parameters obtained for the as-received and laser-treated Mg-1Zn-1Ca and Mg-3Zn-0.4Ca alloys after different immersion times are shown in Figure 13.

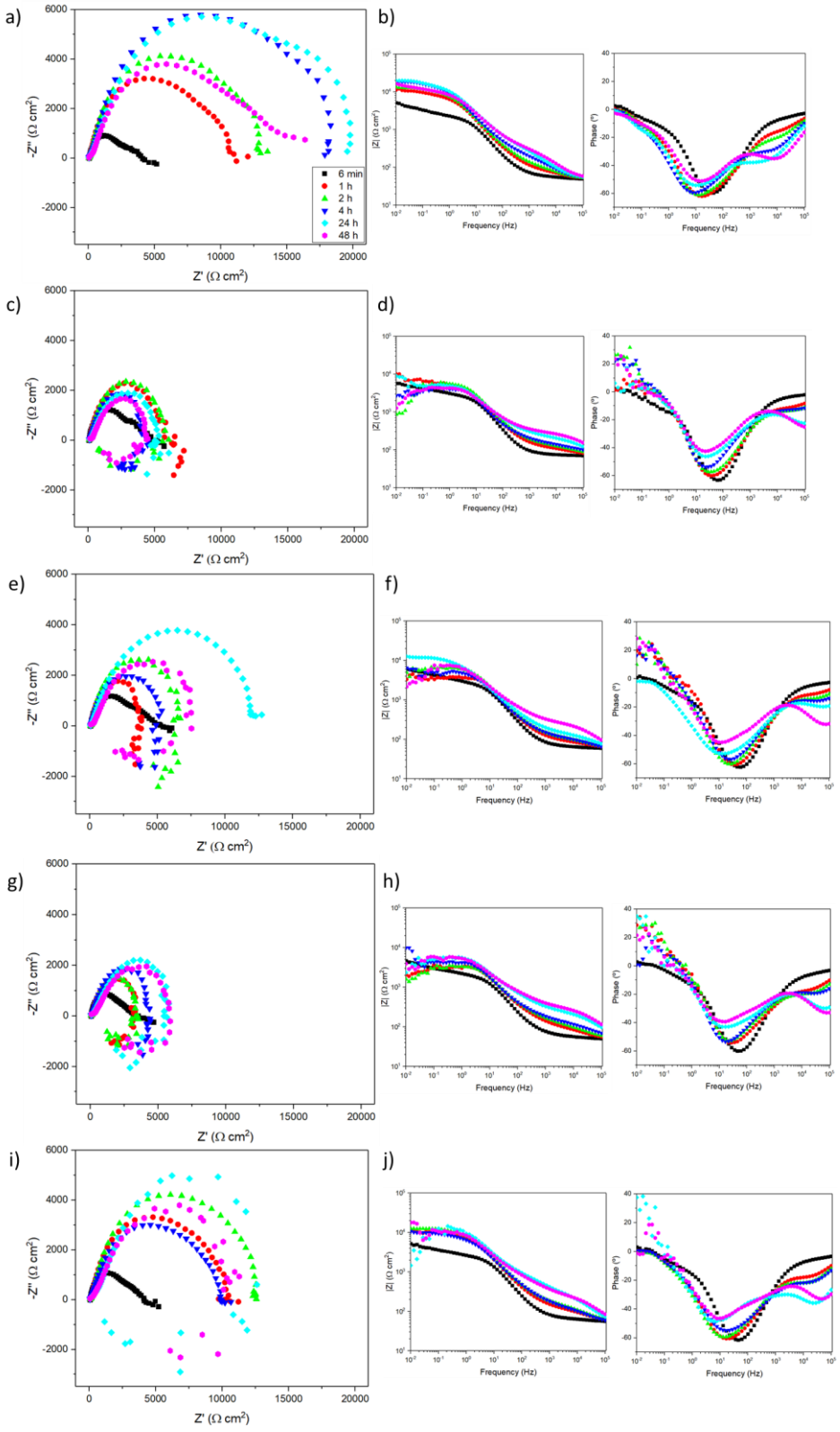

Figure 10. Nyquist (a, c, e, g, i) and Bode (b, d, f, h, j) plots of the EIS spectra of Mg-1Zn-1Ca alloy: (a-b) as-received, (c-d) 75 mm s^{-1}, (e-f) 80 mm s^{-1}, (g-h) 85 mm s^{-1} and (i-j) 90 mm s^{-1}.

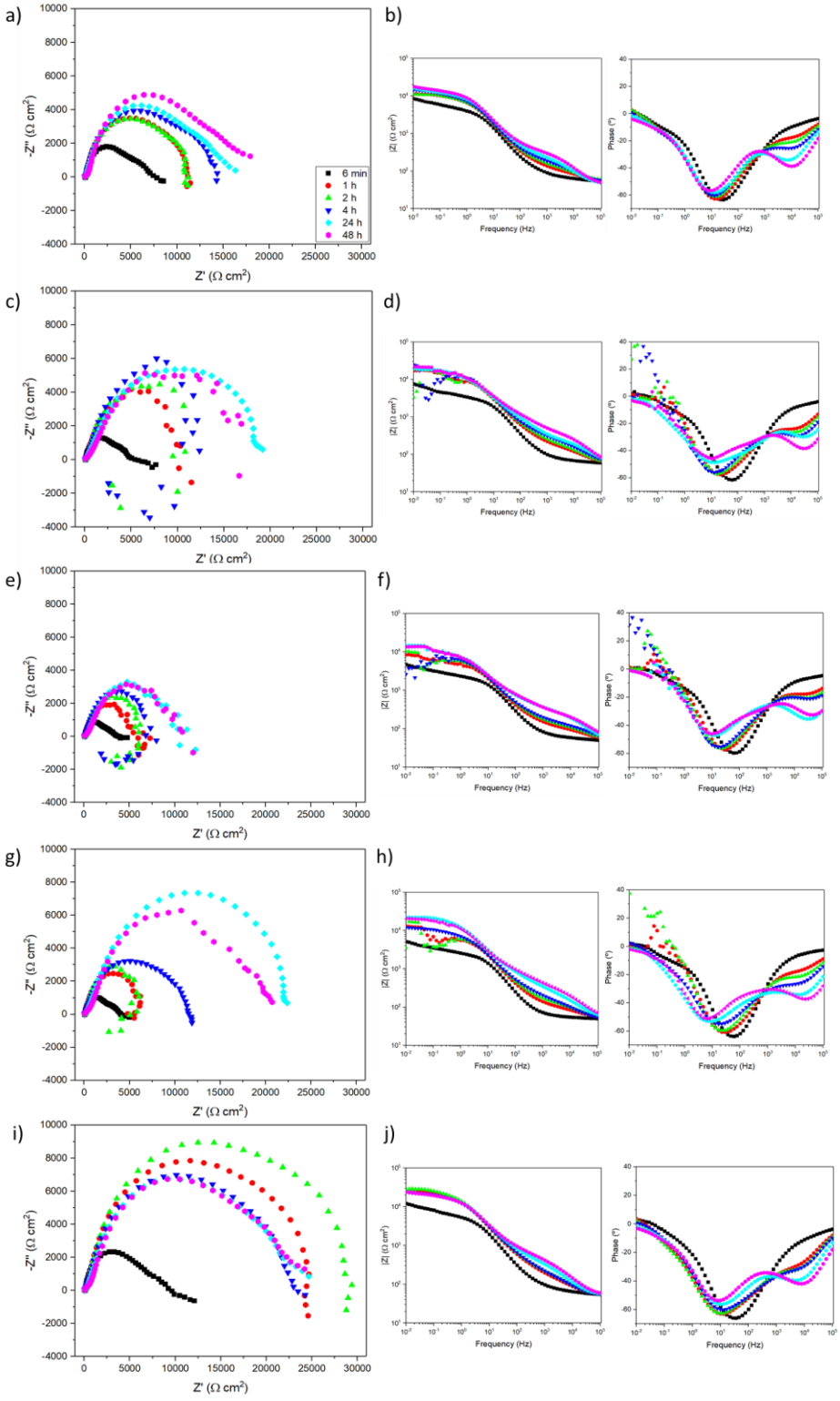

Figure 11. Nyquist (a, c, e, g, i) and Bode (b, d, f, h, j) plots of the EIS spectra of Mg-3Zn-0.4Ca alloy: (a-b) as-received, (c-d) 75 mm s^{-1}, (e-f) 80 mm s^{-1}, (g-h) 85 mm s^{-1} and (i-j) 90 mm s^{-1}.

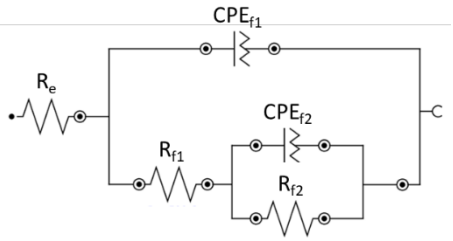

Figure 12. Equivalent electrical circuit model used to simulate the impedance spectra at limited frequency range of the Mg-1Zn-1Ca and Mg-3Zn-0.4Ca alloys in the as-received condition and after laser treatment at different immersion times in Hanks' solution at room temperature: 1h, 2h, 4h, 24 h and 48 h.

For both alloys, R_{f1} increases with immersion time. As observed in Figure 13a, the resistance of the semi-protective layer in the Mg-1Zn-1Ca alloy is higher in the samples treated at higher scanning speeds at 48 h. This result also agrees with the ones obtained for the Mg-3Zn-0.4Ca alloy (Figure 13b). Furthermore, after 48 h of immersion in Hanks' solution all the laser-treated specimens showed higher resistance values of this layer compared to the as-received condition. Laser treatment promotes the formation of a more protective layer at longer immersion times. Regarding the characteristic MgO film formed on the Mg substrates immersed in an aqueous media (Figures 13 c and d), its resistance tends to stabilize after 4 h of immersion for all samples. For the Mg-1Zn-1Ca alloy, the layer formed on the as-received sample presented the highest resistance, while for the Mg-3Zn-0.4Ca alloy, the protective layer formed on the samples treated at higher scanning speeds showed higher resistance values. The resistance of both protective layers was found to be higher in the Mg-3Zn-0.4Ca alloy than in the Mg-1Zn-1Ca alloy. These results indicate the beneficial effect of the HPDL treatments at

higher scanning speeds on the corrosion resistance of the Mg-based alloys. As occurred in the microhardness study, LSM treatments did not lead to the higher corrosion resistance values. The SLSM of the secondary phases was enough to produce an improvement in the corrosion behaviour.

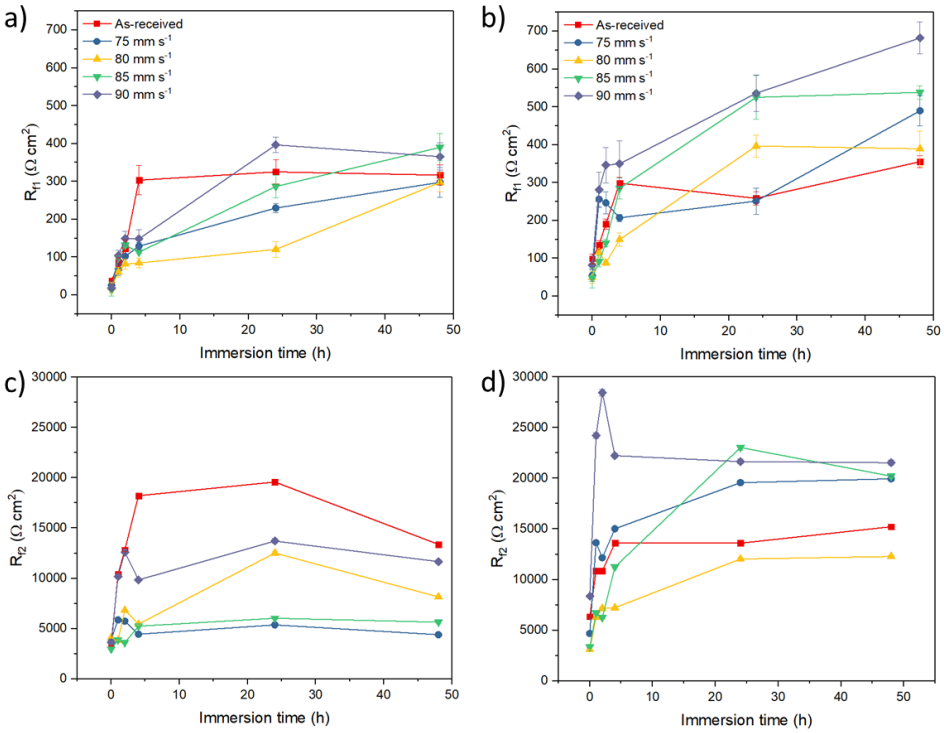

Figure 13. Evolution of the R_{f1} and R_{f2} with immersion time for: (a),(c) Mg-1Zn-1Ca alloy and (b),(d) Mg-3Zn-0.4Ca alloy, in the as-received state and laser-treated conditions at different scanning speeds.

4. Conclusions

In this research, the effect of the laser treatment on the microstructure, hardness and corrosion behaviour of two different Mg-Zn-Ca alloys (Mg-1Zn-1Ca and Mg-3Zn-0.4Ca) have been analysed in order to evaluate the suitability of these alloys to be used as biodegradable implants.

The following conclusions can be drawn:

1. The laser treatment modified the microstructure of the Mg-1Zn-1Ca and Mg-3Zn-0.4Ca alloys. Depending on the laser parameters used, the complete laser surface melting (LSM) or the selective laser surface melting (SLSM) was reached. For the same laser input energy, the Mg-1Zn-1Ca alloy suffered greater microstructural changes than the Mg-3Zn-0.4Ca alloy.
2. The laser treatment produced an increase in the microhardness. For the Mg-1Zn-1Ca the microhardness grew from 13 % to 24 %, while in the Mg-3Zn-0.4Ca the microhardness was improved by 11 % – 27 %, depending on the laser parameters. SLSM caused the greatest hardness increases in the alloys.
3. A reduction in the corrosion rates of these Mg-Zn-Ca alloys for 336 h after laser treatment was reached, showing the effectiveness of the HPDL surface treatments. The corrosion progress in the laser-treated Mg-1Zn-1Ca samples took place through the secondary phases formed after laser treatment. For the Mg-3Zn-0.4Ca alloy, the corrosion advanced through the α-Mg matrix in the laser-treated samples, remaining the $Ca_2Mg_6Zn_3$ phase unaffected by the corrosion.
4. The 80 mm s^{-1} laser-treated Mg-1Zn-1Ca alloy presents the lowest value of hydrogen evolved and an increase of hardness with respect to the as-cast Mg-1Zn-1Ca alloy. For the Mg-3Zn-0.4Ca alloy, at 75 mm s^{-1}, the hardness is improved, and the corrosion rate is lower than in the rest of the studied conditions.

Acknowledgements

The authors would like to acknowledge the financial support from the Agencia Estatal de Investigación (Project RTI2018-096391-B-C31), Comunidad de Madrid (Project ADITIMAT-CM S2018/NMT-4411) and the FPU grant (15/03606) from the Ministerio de Educación, Cultura y Deporte, Spain. Authors acknowledge the Magnesium Innovation Centre MagIC and the WZK department (Germany) for hosting N. Pulido-González for a pre-doctoral fellowship.

References

[1] M. Mohedano, B.J.C. Luthringer, B. Mingo, F. Feyerabend, R. Arrabal, P.J. Sanchez-Egido, C. Blawert, R. Willumeit-Römer, M.L. Zheludkevich, E. Matykina, Bioactive plasma electrolytic oxidation coatings on Mg-Ca alloy to control degradation behaviour, Surf. Coatings Technol. 315 (2017) 454–467. https://doi.org/10.1016/j.surfcoat.2017.02.050.

[2] S. V. Lamaka, M.F. Montemor, A.F. Galio, M.L. Zheludkevich, C. Trindade, L.F. Dick, M.G.S. Ferreira, Novel hybrid sol-gel coatings for corrosion protection of AZ31B magnesium alloy, Electrochim. Acta. 53 (2008) 4773–4783. https://doi.org/10.1016/j.electacta.2008.02.015.

[3] S. Kaabi Falahieh Asl, S. Nemeth, M.J. Tan, Mechanism of calcium phosphate deposition in a hydrothermal coating process, Surf. Coatings Technol. 270 (2015) 197–205. https://doi.org/10.1016/j.surfcoat.2015.03.003.

[4] Y. Ding, C. Wen, P. Hodgson, Y. Li, Effects of alloying elements on the corrosion

behavior and biocompatibility of biodegradable magnesium alloys: A review, J. Mater. Chem. B. 2 (2014) 1912–1933. https://doi.org/10.1039/c3tb21746a.

[5] K. Gusieva, C.H.J. Davies, J.R. Scully, N. Birbilis, Corrosion of magnesium alloys: the role of alloying, Int. Mater. Rev. 60 (2015) 169–194. https://doi.org/10.1179/1743280414Y.0000000046.

[6] M. Esmaily, J.E. Svensson, S. Fajardo, N. Birbilis, G.S. Frankel, S. Virtanen, R. Arrabal, S. Thomas, L.G. Johansson, Fundamentals and advances in magnesium alloy corrosion, Prog. Mater. Sci. 89 (2017) 92–193. https://doi.org/10.1016/j.pmatsci.2017.04.011.

[7] L. Katsarou, K. Suresh, K.P.P. Rao, N. Hort, C. Blawert, C.L.L. Mendis, H. Dieringa, Microstructure and properties of magnesium alloy Mg-1Zn-1Ca (Zx11), 2015. https://doi.org/10.1007/978-3-319-48185-2_78.

[8] H.R. Bakhsheshi-Rad, M.R. Abdul-Kadir, M.H. Idris, S. Farahany, Relationship between the corrosion behavior and the thermal characteristics and microstructure of Mg-0.5Ca-xZn alloys, Corros. Sci. 64 (2012) 184–197. https://doi.org/10.1016/j.corsci.2012.07.015.

[9] D. Zander, N.A. Zumdick, Influence of Ca and Zn on the microstructure and corrosion of biodegradable Mg-Ca-Zn alloys, Corros. Sci. 93 (2015) 222–233. https://doi.org/10.1016/j.corsci.2015.01.027.

[10] H. Ibrahim, A.D. Klarner, B. Poorganji, D. Dean, A.A. Luo, M. Elahinia, Microstructural, mechanical and corrosion characteristics of heat-treated Mg-1.2Zn-0.5Ca (wt%) alloy for use as resorbable bone fixation material, J. Mech.

Behav. Biomed. Mater. 69 (2017) 203–212. https://doi.org/10.1016/j.jmbbm.2017.01.005.

[11] D.C. Eastwood, H. Ibrahim, S. Moghaddam, M. Elahinia, “Mechanical and In Vitro Corrosion Properties of a Heat-Treated Mg-Zn-Ca-Mn Alloy as a Potential Bioresorbable Material,” 2017. https://doi.org/10.1021/bk-2014-1158.ch005.

[12] W. li Cheng, S. chao Ma, Y. Bai, Z. qin Cui, H. xia Wang, Corrosion behavior of Mg-6Bi-2Sn alloy in the simulated body fluid solution: The influence of microstructural characteristics, J. Alloys Compd. 731 (2018) 945–954. https://doi.org/10.1016/j.jallcom.2017.10.073.

[13] F. Witte, N. Hort, C. Vogt, S. Cohen, K.U. Kainer, R. Willumeit, F. Feyerabend, Degradable biomaterials based on magnesium corrosion, Curr. Opin. Solid State Mater. Sci. 12 (2008) 63–72. https://doi.org/10.1016/j.cossms.2009.04.001.

[14] M.A. Pinto, N. Cheung, M.C.F. Ierardi, A. Garcia, Microstructural and hardness investigation of an aluminum-copper alloy processed by laser surface melting, Mater. Charact. 50 (2003) 249–253. https://doi.org/10.1016/S1044-5803(03)00091-3.

[15] L.M. Laorden, P. Rodrigo, B. Torres, J. Rams, Modification of microstructure and superficial properties of A356 and A356/10%SiCp by Selective Laser Surface Melting (SLSM), Surf. Coatings Technol. 309 (2017) 1001–1009. https://doi.org/10.1016/j.surfcoat.2016.10.046.

[16] J. Rams, A. Pardo, A. Ureña, R. Arrabal, F. Viejo, A.J. López, Surface treatment of aluminum matrix composites using a high power diode laser, Surf. Coatings

Technol. 202 (2007) 1199–1203. https://doi.org/10.1016/j.surfcoat.2007.05.048.

[17] F. Bachmann, Industrial applications of high power diode lasers in materials processing, Appl. Surf. Sci. 208–209 (2003) 125–136. https://doi.org/10.1016/S0169-4332(02)01349-1.

[18] F. Viejo, A. Pardo, J. Rams, M.C. Merino, A.E. Coy, R. Arrabal, E. Matykina, High power diode laser treatments for improving corrosion resistance of A380/SiCp aluminium composites, Surf. Coatings Technol. 202 (2008) 4291–4301. https://doi.org/10.1016/j.surfcoat.2008.03.025.

[19] C. Taltavull, B. Torres, A.J. López, P. Rodrigo, E. Otero, J. Rams, Selective laser surface melting of a magnesium-aluminium alloy, Mater. Lett. 85 (2012) 98–101. https://doi.org/10.1016/j.matlet.2012.07.004.

[20] C. Taltavull, B. Torres, A.J. López, P. Rodrigo, J. Rams, Novel laser surface treatments on AZ91 magnesium alloy, Surf. Coatings Technol. 222 (2013) 118–127. https://doi.org/10.1016/j.surfcoat.2013.02.013.

[21] C. Taltavull, B. Torres, A.J. Lopez, P. Rodrigo, E. Otero, A. Atrens, J. Rams, Corrosion behaviour of laser surface melted magnesium alloy AZ91D, Mater. Des. 57 (2014) 40–50. https://doi.org/10.1016/j.matdes.2013.12.069.

[22] C. Taltavull, A.J. López, B. Torres, J. Rams, Fracture behaviour of a magnesium – aluminium alloy treated by selective laser surface melting treatment, J. Mater. 55 (2014) 361–365. https://doi.org/10.1016/j.matdes.2013.10.010.

[23] Y.C. Guan, W. Zhou, H.Y. Zheng, Effect of laser surface melting on corrosion

behaviour of AZ91D Mg alloy in simulated-modified body fluid, J. Appl. Electrochem. 39 (2009) 1457–1464. https://doi.org/10.1007/s10800-009-9825-2.

[24] B. Manne, H. Thiruvayapati, S. Bontha, R. Motagondanahalli Rangarasaiah, M. Das, V.K. Balla, Surface design of Mg-Zn alloy temporary orthopaedic implants: Tailoring wettability and biodegradability using laser surface melting, Surf. Coatings Technol. 347 (2018) 337–349. https://doi.org/10.1016/j.surfcoat.2018.05.017.

[25] R. K.R., S. Bontha, R. M.R., M. Das, V.K. Balla, Laser surface melting of Mg-Zn-Dy alloy for better wettability and corrosion resistance for biodegradable implant applications, Appl. Surf. Sci. 480 (2019) 70–82. https://doi.org/10.1016/j.apsusc.2019.02.167.

[26] C. Ma, G. Peng, L. Nie, H. Liu, Y. Guan, Laser surface modification of Mg-Gd-Ca alloy for corrosion resistance and biocompatibility enhancement, Appl. Surf. Sci. 445 (2018) 211–216. https://doi.org/10.1016/j.apsusc.2018.03.174.

[27] J. Zhang, Y. Guan, W. Lin, X. Gu, Enhanced mechanical properties and biocompatibility of Mg-Gd-Ca alloy by laser surface processing, Surf. Coatings Technol. 362 (2019) 176–184. https://doi.org/10.1016/j.surfcoat.2019.01.063.

[28] R. Xu, M.C. Zhao, Y.C. Zhao, L. Liu, C. Liu, C. Gao, C. Shuai, A. Atrens, Improved biodegradation resistance by grain refinement of novel antibacterial ZK30-Cu alloys produced via selective laser melting, Mater. Lett. 237 (2019) 253–257. https://doi.org/10.1016/j.matlet.2018.11.071.

[29] J.Z. Lu, S.S. Joshi, M. V. Pantawane, Y.H. Ho, T.C. Wu, N.B. Dahotre, Optimization of biocompatibility in a laser surface treated Mg-AZ31B alloy, Mater. Sci. Eng. C. 105 (2019) 110028. https://doi.org/10.1016/j.msec.2019.110028.

[30] J. Suchy, M. Horynová, L. Klakurková, D. Palousek, D. Koutny, L. Celko, Effect of Laser Parameters on Processing of Biodegradable Magnesium Alloy WE43 via Selective Laser Melting Method, (2020). https://doi.org/https://doi.org/10.3390/ma13112623.

[31] T. Guan, S. Chen, X. Chen, J. Liang, C. Liu, M. Wang, Effect of laser incident energy on microstructures and mechanical properties of 12CrNi2Y alloy steel by direct laser deposition, J. Mater. Sci. Technol. 35 (2019) 395–402. https://doi.org/10.1016/j.jmst.2018.10.024.

[32] Z. Shi, A. Atrens, An innovative specimen configuration for the study of Mg corrosion, Corros. Sci. 53 (2011) 226–246. https://doi.org/10.1016/j.corsci.2010.09.016.

[33] N. Pulido-González, B. Torres, S. García-Rodríguez, P. Rodrigo, V. Bonache, P. Hidalgo-Manrique, M. Mohedano, J. Rams, Mg–1Zn–1Ca alloy for biomedical applications. Influence of the secondary phases on the mechanical and corrosion behaviour, J. Alloys Compd. 831 (2020) 1–15. https://doi.org/10.1016/j.jallcom.2020.154735.

[34] N. Pulido-González, B. Torres, P. Rodrigo, N. Hort, J. Rams, Microstructural, mechanical and corrosion characterization of an as-cast Mg–3Zn–0.4Ca alloy for biomedical applications, J. Magnes. Alloy. 8 (2020) 510–522. https://doi.org/10.1016/j.jma.2020.02.007.

[35] D. Liu, Y. Liu, Y. Huang, R. Song, M. Chen, Effects of solidification cooling rate on the corrosion resistance of Mg-Zn-Ca alloy, Prog. Nat. Sci. Mater. Int. 24 (2014) 452–457. https://doi.org/10.1016/j.pnsc.2014.08.002.

[36] M. Hradilová, D. Vojtěch, J. Kubásek, J. Čapek, M. Vlach, Structural and mechanical characteristics of Mg-4Zn and Mg-4Zn-0.4Ca alloys after different thermal and mechanical processing routes, Mater. Sci. Eng. A. 586 (2013) 284–291. https://doi.org/10.1016/j.msea.2013.08.008.

[37] J. Chen, Y. Sun, J. Zhang, W. Cheng, X. Niu, C. Xu, Effects of Ti addition on the microstructure and mechanical properties of Mg-Zn-Zr-Ca alloys, J. Magnes. Alloy. 3 (2015) 121–126. https://doi.org/10.1016/j.jma.2015.05.001.

[38] Q. Zhang, L. Tong, L. Cheng, Z. Jiang, J. Meng, H. Zhang, Effect of Ce/La microalloying on microstructural evolution of Mg-Zn-Ca alloy during solution treatment, J. Rare Earths. 33 (2015) 70–76. https://doi.org/10.1016/S1002-0721(14)60385-9.

[39] K.P. Rao, K. Suresh, Y.V.R.K. Prasad, C. Dharmendra, N. Hort, H. Dieringa, High temperature strength and hot working technology for As-cast Mg-1Zn-1Ca (ZX11) alloy, Metals (Basel). 7 (2017). https://doi.org/10.3390/met7100405.

[40] S. Wang, Y. Zhao, H. Guo, F. Lan, H. Hou, Mechanical and thermal conductivity properties of enhanced phases in Mg-Zn-Zr system from first principles, Materials (Basel). 11 (2018). https://doi.org/10.3390/ma11102010.

[41] G. Yuan, G. You, S. Bai, W. Guo, Effects of heat treatment on the thermal properties of AZ91D magnesium alloys in different casting processes, J. Alloys

Compd. 766 (2018) 410–416. https://doi.org/10.1016/j.jallcom.2018.06.370.

[42] S. Li, X. Yang, J. Hou, W. Du, A review on thermal conductivity of magnesium and its alloys, J. Magnes. Alloy. 8 (2020) 78–90. https://doi.org/10.1016/j.jma.2019.08.002.

[43] F. Shi, C. Wang, X. Guo, Microstructures and properties of as-cast Mg92Zn4Y4 and Mg92Zn4Y3Gd1 alloys with LPSO phase, Xiyou Jinshu Cailiao Yu Gongcheng/Rare Met. Mater. Eng. 44 (2015) 1617–1622. https://doi.org/10.1016/s1875-5372(15)30103-x.

[44] F. Zhang, A. Ma, D. Song, J. Jiang, F. Lu, L. Zhang, D. Yang, J. Chen, Improving in-vitro biocorrosion resistance of Mg-Zn-Mn-Ca alloy in Hank's solution through addition of cerium, J. Rare Earths. 33 (2015) 93–101. https://doi.org/10.1016/S1002-0721(14)60388-4.

[45] Z. Chun-Yan, Z. Rong-Chang, L. Cheng-Long, G. Jia-Cheng, Comparison of calcium phosphate coatings on Mg-Al and Mg-Ca alloys and their corrosion behavior in Hank's solution, Surf. Coatings Technol. 204 (2010) 3636–3640. https://doi.org/10.1016/j.surfcoat.2010.04.038.

[46] D. Song, G. Guo, J. Jiang, L. Zhang, A. Ma, X. Ma, J. Chen, Z. Cheng, Hydrothermal synthesis and corrosion behavior of the protective coating on Mg-2Zn-Mn-Ca-Ce alloy, Prog. Nat. Sci. Mater. Int. 26 (2016) 590–599. https://doi.org/10.1016/j.pnsc.2016.11.002.

[47] N.I. Zainal Abidin, A.D.A. Atrens, D. Martin, A.D.A. Atrens, Corrosion of high purity Mg, Mg2Zn0.2Mn, ZE41 and AZ91 in Hank's solution at 37°C, Corros. Sci.

53 (2011) 3542–3556. https://doi.org/10.1016/j.corsci.2011.06.030.

[48] V. Shkirskiy, A.D. King, O. Gharbi, P. Volovitch, J.R. Scully, K. Ogle, N. Birbilis, Revisiting the electrochemical impedance spectroscopy of magnesium with online inductively coupled plasma atomic emission spectroscopy, ChemPhysChem. 16 (2015) 536–539. https://doi.org/10.1002/cphc.201402666.

[49] D. Mei, S. V. Lamaka, C. Feiler, M.L. Zheludkevich, The effect of small-molecule bio-relevant organic components at low concentration on the corrosion of commercially pure Mg and Mg-0.8Ca alloy: An overall perspective, Corros. Sci. 153 (2019) 258–271. https://doi.org/10.1016/j.corsci.2019.03.039.

[50] D. Mei, S. V. Lamaka, J. Gonzalez, F. Feyerabend, R. Willumeit-Römer, M.L. Zheludkevich, The role of individual components of simulated body fluid on the corrosion behavior of commercially pure Mg, Corros. Sci. 147 (2019) 81–93. https://doi.org/10.1016/j.corsci.2018.11.011.